De Dominicis et al. *EPJ Quantum Technology* (2026) 13:47
https://doi.org/10.1140/epjqt/s40507-026-00490-2

EPJ.org

EPJ Quantum Technology

RESEARCH Open Access

Evaluating radiation impact on transmon qubits in above and underground facilities

Francesco De Dominicis[1,2†], Tanay Roy[3*†], Ambra Mariani[4*], Mustafa Bal[5], Camilla Bonomo[4,6], Nicola Casali[4], Ivan Colantoni[7,4], Francesco Crisa[8], Angelo Cruciani[4], Fernando Ferroni[1,4], Dounia L. Helis[2], Lorenzo Pagnanini[1,2], Valerio Pettinacci[4], Roman Pilipenko[5], Stefano Pirro[2], Andrei Puiu[2], Alberto Ressa[4], Alexander Romanenko[5], Marco Vignati[4,6], David van Zanten[5], Shaojiang Zhu[5], Anna Grassellino[5] and Laura Cardani[4]

*Correspondence: roytanay@fnal.gov; ambra.mariani@roma1.infn.it
[3]Superconducting Quantum Materials and Systems Center (SQMS), Fermi National Accelerator Laboratory, Batavia, IL 60510, USA
[4]Sezione di Roma, INFN, Rome, I-00185, Italy
Full list of author information is available at the end of the article
†Equal contributors

Abstract

Superconducting qubits can be sensitive to energy deposits caused by cosmic rays and ambient radioactivity. While previous studies have explored correlated effects in time and space due to cosmic ray interactions, we present the first direct comparison of a transmon qubit's performance measured at two distinct sites: the above-ground SQMS facility (Fermilab, US) and the deep-underground Gran Sasso Laboratory (Italy). Despite the stark difference in radiation levels, we observe a similar average qubit relaxation time of approximately 80 microseconds at both locations. To investigate radiation-induced events, we employ a fast decay detection protocol, comparing the relative rates of events between the two environments. Although intrinsic noise remains the dominant source of errors in superconducting qubits, our analysis revealed a significant excess of radiation-induced events for high-coherence transmon qubits operated above-ground. Finally, using γ-ray sources with increasing activity levels, we evaluate the qubit response in a controlled low-background environment.

Keywords: Superconducting qubits; Transmon qubits; Ionizing radiation; Cosmic rays; Gamma rays; Radiation-induced errors

1 Introduction

Over the past decades, superconducting circuits have emerged as a leading technology for applications in quantum information [1–6], photon, and particle detection [7–18]. In recent years, several research groups have started investigating the impact of particle interactions on the performance of superconducting quantum bits (qubits) with different geometries and materials [19, 20], and recent work has introduced techniques for fast T_1 monitoring [21]. For example, it has been observed that the lifetime of a transmon qubit can decrease when exposed to high levels of radiation [22]. Additionally, the effect of high energy deposits can rapidly propagate from the initial location of deposition, inducing correlated errors or even general system failure [23, 24]. Wilen et al. [25] found that the rate of charge jumps in an array of charge-sensitive qubits (operated as electrometers) was consistent with the expected rate of interactions from ambient radioactivity and cosmic rays. In contrast, Thorbeck et al. [26] observed no significant direct effects from radiation, but suggested that ionizing radiation may interact with two-level systems (TLSs), a dominant noise source in superconducting qubits [27–34].

Other studies have shown that suppressing radioactivity can enhance the performance of superconducting circuits. Operating devices in low-background facilities reduces correlated errors [35], stabilizes fluxonium qubits [36], and improves the internal quality factor of superconducting resonators [37]. The latter publication also determined that the substrate on which qubits are deposited, rather than the qubits themselves, is the primary target for particle interactions.

These findings have motivated efforts in further directions aimed at studying and mitigating possible effects of radioactivity and cosmic rays. Promising results have been achieved by equipping the chip with "traps" designed to absorb phonons produced (also) by radioactive interactions [38–40], and using gap engineering [20, 41, 42]. Other approaches focus on minimizing radiation from qubit construction materials, such as Printed Circuit Boards (PCBs), which have been shown to produce a sizeable rate of events in the qubit chip [43]. Furthermore, it is also worth mentioning recent proposals of equipping qubits with particle detection systems [44] or external muon detectors [24, 42, 45, 46].

In this work, we present the first study of a charge-insensitive transmon qubit with energy relaxation time T_1 of the order of 0.1 milliseconds, measured in two laboratories with markedly different radiation levels: the *Quantum Garage* of the Superconducting Quantum Materials and Systems (SQMS) Center at Fermilab (FNAL, Illinois, US), and the *Ieti Facility* located in the deep-underground Gran Sasso National Laboratory of INFN (LNGS, L'Aquila, Italy). All measurements were performed on the same qubit, enabling a direct comparison between the above-ground and deep-underground environments. The aim of this study is to quantify the impact of cosmic radiation and environmental radioactivity on the qubit.

The paper is structured as follows. To understand how different radiation environments affect qubit performance, we first compare the average relaxation time of this qubit above ground at FNAL and deep underground at LNGS (Sects. 2.1–2.2). Our results show that, as expected, radiation has a negligible effect even on transmons with a relaxation time of 0.1 milliseconds. By developing a fast decay detection protocol with active reset and a novel analysis technique, we are able to disentangle radiation-induced events (Sects. 2.3–2.4). We systematically explore how various experimental parameters—such as qubit relaxation time and the sampling period of the fast reset—influence the results. We find that radiation-induced event rates are significantly higher at FNAL compared to LNGS. Finally, we expose the superconducting chip to calibrated γ-ray sources in a controlled, low-background environment, to further characterize the qubit's response to radiation and validate our findings (Sect. 2.5).

2 Results

2.1 Device and experimental locations

The chip consisted of a 432 μm thick HEMEX grade Sapphire substrate with dimensions of 7.5×7.5 mm^2. The entire substrate was covered in Niobium, which creates a ground plane that may act as a phonon trap, diminishing phonon propagation and absorption in the active part of the qubit [48, 49]. Eight fixed-frequency Niobium transmons with different geometries and standard Al/AlOx/Al Josephson junctions were deposited on the

Table 1 Expected rate of interactions in the Sapphire substrate at the two experimental locations. The expected interaction rates were obtained by scaling the simulation results using both measured and theoretical inputs. Specifically, the γ-ray flux in the experimental rooms were measured with a 3″ portable NaI spectrometer, yielding (1.7 ± 0.9) γ/cm^2/sec at FNAL and (1.0 ± 0.5) γ/cm^2/sec at LNGS. For muons, a flux of 1 μ/cm^2/min was assumed at FNAL, based on the site altitude, while a six-order-of-magnitude suppression factor was applied to estimate the flux at LNGS [47]. Lastly, the radioactive contamination of the experimental setup components was measured in Ref. [43]

Source	FNAL [events/sec]	LNGS [events/sec]
Lab γ-ray	$(31 \pm 2) \times 10^{-3}$	$(1.3 \pm 0.1) \times 10^{-3}$
Muons	$(8 \pm 0.5) \times 10^{-3}$	$<10^{-5}$
Setup	$(2.7 \pm 0.5) \times 10^{-3}$	$(2.7 \pm 0.5) \times 10^{-3}$
Total	$(42 \pm 3) \times 10^{-3}$	$(4.0 \pm 0.6) \times 10^{-3}$

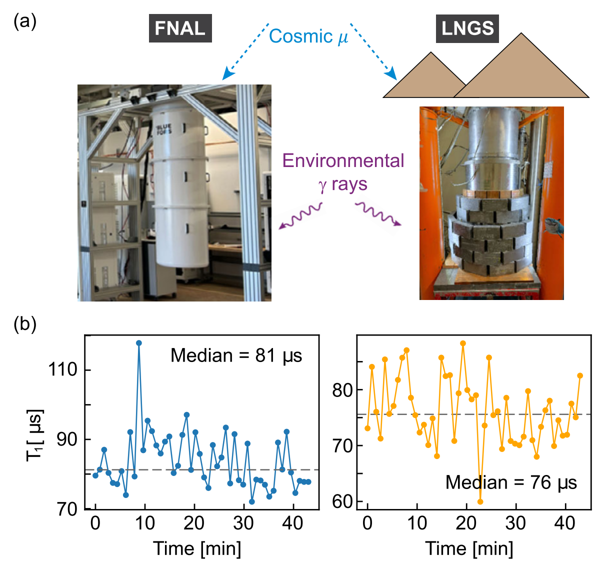

Figure 1 Comparison of the two experimental sites. (a) The above-ground cryostat at FNAL is exposed to environmental radiation and cosmic-rays, whereas the deep-underground cryostat at LNGS is strongly guarded from cosmic muons by the 1.4 km deep rock overburden and from environmental γ-rays through a Copper plus Lead shielding. (b) The left and right panels display data taken at FNAL and LNGS, respectively. Standard T_1 measurements performed on the same device show similar fluctuations at both sites. However, these measurements are too slow to detect rapid T_1 drops at millisecond time scales potentially due to radiation impact

chip, as detailed in Supplementary Section A. To mitigate losses caused by the formation of Nb_2O_5, the qubits' surfaces were capped with a ∼10 nm thick layer of Gold [50]. This capping technique allowed us to achieve long T_1 values, ranging from tens up to hundreds of microseconds, an essential feature for observing relaxation time variations on microsecond timescales.

To predict the rate of hits due to ionizing radiation, we performed a Monte Carlo simulation using the GEANT4 framework [51] developed in Ref. [43]. We anticipate the total rate of radiation events interacting within the chip at FNAL and LNGS to be $(42 \pm 3) \times 10^{-3}$ events/sec and $(4.0 \pm 0.6) \times 10^{-3}$ events/sec, respectively. Table 1 summarizes the simulation results, with detailed information provided in Supplementary Section B. At FNAL (Fig. 1(a), left panel), the rate of impacts in the Sapphire substrate is dominated by γ-rays from naturally occurring radioactive isotopes, with cosmic-ray muons also contributing significantly. At LNGS (Fig. 1(a), right panel), muon interactions are reduced by six orders of magnitude due to the 1.4 km rock overburden, and gamma radiation is minimized by Copper and Lead shields, installed both inside and around the cryostat. The last source of radiation arises from the materials of the chip and its surrounding components. In a prior study within the SQMS *Round Robin* project [43], we measured the radioactive content of each component and determined that cables, connectors, amplifiers, and circulators contribute negligibly to the overall rate. However, the PCBs, located near the chip, exhibits significant radioactive contamination. This contribution dominates the "Setup" rates in Table 1 and, while negligible at FNAL, becomes the primary source at LNGS where external radiation is highly suppressed.

To explore the impact of elevated radiation levels, at LNGS, we used calibrated Thorium sources to increase the event rate up to one event every two seconds. This allowed us to investigate transmons' behavior in a controlled "high" radiation environment.

2.2 Relaxation time in different environments

When a particle impinges on the qubit chip, it releases energy into the substrate. Muons create long tracks across the chip, while γ-rays interact through photo-electric absorption or (mainly via) Compton scattering, producing short-track electrons. In the absence of an electric field, the thousands of charges created along the ionizing track recombine into phonons, which diffuse throughout the chip [25]. As illustrated in Fig. 2(a), these phonons can break Cooper pairs in superconductors, creating quasiparticles. When these quasiparticles tunnel through the Josephson Junction, they may cause the qubit to lose energy and decay to its ground state $|g\rangle$ [39]. This leads to extended periods during which the relaxation time is strongly reduced, resulting in a significantly lower T_1. Previous studies indicated that these low T_1 periods can last from one to several tens of milliseconds [23, 24].

Transmons with energy relaxation rates of $1/40$ and $1/32\ \mu s^{-1}$ were already characterized in a facility in which radioactivity could be controlled by using a movable lead shield. The authors of the paper, determined that environmental radioactivity was negligible for qubits with that T_1 [22]. In this work, we characterized the 8 qubits and chose to focus on qubit "Q1" (Supplementary Section A), which exhibited the best combination of T_1 ($\sim$80 µs) and readout fidelity ($\sim$90–95%). This compromise makes Q1 particularly well suited for radiation studies, as a longer T_1 increases sensitivity to radiation-induced events, while high readout fidelity ensures reliable event identification.

We performed standard T_1 measurements in both above-ground (FNAL) and underground (LNGS) environments using the same qubit. Each time-delay point was measured over 500 µs (no active reset) and averaged over 1000 repetitions. A total of 101 delay points were acquired per T_1 trace, resulting in an acquisition time of about 50 seconds per data point, as shown in Fig. 1(b). The results showed similar mean values and fluctuations in T_1, consistent with typical transmon behavior [50], and no abrupt T_1 drops were observed. This outcome aligns with expectations, as standard T_1 experiments, due to their averaging nature, lack the temporal resolution necessary to capture millisecond-scale fluctuations. As a consequence, to probe such rapid events, we developed a tailored fast decay detection protocol [20, 23] specifically designed to monitor single qubits with sub-millisecond resolution (Sect. 2.3). Nevertheless, the standard T_1 experiment was performed multiple times: initially at FNAL, then at LNGS, and finally again at FNAL, interleaved with the

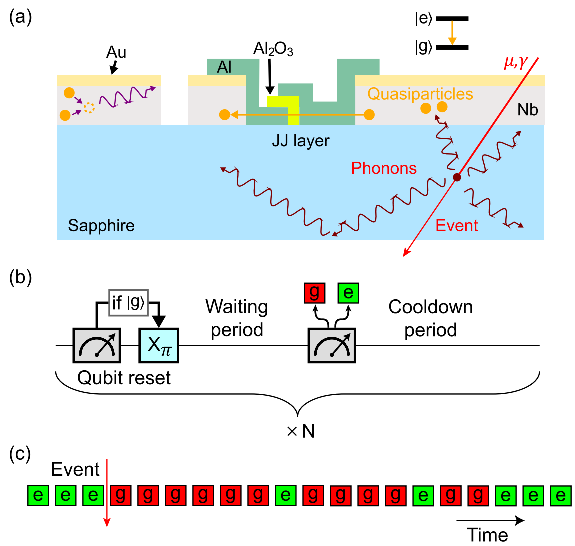

Figure 2 Quasiparticle generation process and experimental protocol. (a) Schematic representation of quasiparticles generation due to particle interactions in the substrate. Ionizing radiation impinging on the substrate produces electron-hole pairs that recombine, creating phonons. These phonons spread throughout the chip and, in superconducting materials, can break Cooper pairs into quasiparticles, which can tunnel across the Josephson Junction inducing decay of the qubit from the excited state $|e\rangle$ to the ground state $|g\rangle$. (b) The fast decay detection protocol consists of repeated cycles of qubit preparation in the excited state, a waiting period, measurement, and cooldown period. Each cycle lasts up to 74 μs, with a waiting time of 5 μs, chosen to optimize the sensitivity to fast decays while maintaining a clear distinction between burst-induced events and the spontaneous qubit decay. (c) During normal operation, the qubit is likely to remain in the excited state due to its long T_1. Radiation events drastically reduce T_1, causing repeated detections in $|g\rangle$. Over time, the qubit gradually recovers its natural T_1. These sequences enable the detection of radiation impacts with sub-millisecond resolution

measurements described in the next section. This allowed us to verify that the qubit behavior remained stable and reproducible throughout the entire data-taking campaign.

2.3 Detection protocol

The detection protocol (Fig. 2(b)) begins by resetting the qubit to its first excited state $|e\rangle$ using a conditional π-pulse, applied after an initial measurement if the qubit is found in the ground state $|g\rangle$. After a waiting period Δt_d, the qubit state is measured again, followed by a cooldown period to allow dissipation of readout-induced heating and prevent excessive population of higher excited states. Specifically, the waiting period was fixed at 5 μs (see Supplementary Section E), with readout pulse durations varying from 5 to 9 μs. The π-pulse duration was negligible ($\sim$200 ns) compared to the relaxation time, and cooldown periods were set between 24 and 58 μs. These parameters were chosen dataset by dataset to optimize both state initialization fidelity and readout efficiency. The total time to complete a cycle can be thought as a sampling period (T_S). Measurements of Q1 were done with T_S increasing from 40 to 74 μs.

Under normal conditions, the qubit predominantly remains in $|e\rangle$ due to its relatively long T_1, with occasional decays to $|g\rangle$ occurring at a probability of $P(g) = (1 - e^{-\Delta t_d/T_1}) \approx \Delta t_d/T_1$. Radiation events, however, significantly reduce T_1, leading to a much higher probability of detecting the qubit in $|g\rangle$. Since the effect of quasiparticles lasts longer than the duration of a single cycle, an event due to radiation typically manifests as consecutive detections in $|g\rangle$, as illustrated in Fig. 2(c).

Table 2 List of datasets. Data collected at LNGS and at FNAL. The table shows both the original acquisition duration and the "live-time" duration after excluding intervals with high $|f\rangle$ population. The improvement in the detection protocol increased the live-time of the FNAL measurements of Q1. Multiple datasets were acquired using the same parameters to assess the reproducibility of the results. Columns T_S and $P(g)$ report, respectively, the sampling period and the probability of detecting the qubit in the $|g\rangle$ state, computed from the ratio of measured 0s over the total records. N_{signal}^{min} is the minimum number of zeros in the Signal region. $N_{control}^{min}$ and $N_{control}^{max}$ are the minimum and maximum number of zeros in the Control region. The last column shows the rate of events that passed the data selection

Datasets	Acquisition Time [min]	Live-time [min]	T_S [μs]	$P(g)$ [%]	N_{signal}^{min}	$N_{control}^{min,max}$	Measured Rate [events/sec]
LNGS							
Shielded chip	736.7	209.96	73.6	11.8	19	6, 21	$(0.40 \pm 0.18)\times 10^{-3}$
44 kBq Th Source	620.7	114.0	67.6	14.5	21	8, 24	$(16.0 \pm 1.5)\times 10^{-3}$
76 kBq Th Source	124.1	46.3	67.6	13.8	21	7, 23	$(16.6 \pm 2.5)\times 10^{-3}$
125 kBq Th Source	62.1	23.7	67.6	15.5	22	9, 25	$(26.8 \pm 4.4)\times 10^{-3}$
161 kBq Th Source	62.1	62.1	67.6	14.9	21	8, 25	$(29.4 \pm 2.8)\times 10^{-3}$
FNAL							
60 μs - run1	240.0	55.0	60.0	14.7	21	8, 23	$(7.9 \pm 1.5)\times 10^{-3}$
60 μs - run2	240.0	180.0	60.0	15.8	22	9, 24	$(6.47 \pm 0.77)\times 10^{-3}$
60 μs - run3	130.0	90.0	60.0	15.5	22	9, 24	$(7.9 \pm 1.0)\times 10^{-3}$
68 μs - run1	270.4	270.4	67.6	14.2	21	8, 23	$(5.26 \pm 0.80)\times 10^{-3}$
68 μs - run2	270.4	270.4	67.6	14.3	21	8, 24	$(5.73 \pm 0.59)\times 10^{-3}$
68 μs - run3	270.4	270.4	67.6	13.5	20	7, 23	$(5.79 \pm 0.60)\times 10^{-3}$
74 μs - run1	294.4	294.4	73.6	15.1	21	9, 25	$(5.32 \pm 0.55)\times 10^{-3}$
74 μs - run2	294.4	294.4	73.6	14.5	21	8, 24	$(4.47 \pm 0.50)\times 10^{-3}$
74 μs - run3	294.4	294.4	73.6	14.2	21	8, 23	$(4.98 \pm 0.53)\times 10^{-3}$
74 μs - run4	294.4	294.4	73.6	15.0	21	8, 24	$(4.13 \pm 0.48)\times 10^{-3}$
50 μs - run1	200.0	200.0	50.0	16.0	22	9, 26	$(8.33 \pm 0.83)\times 10^{-3}$
50 μs - run2	200.0	200.0	50.0	16.3	22	9, 26	$(8.58 \pm 0.85)\times 10^{-3}$
50 μs - run3	200.0	200.0	50.0	17.6	23	11, 28	$(9.08 \pm 0.87)\times 10^{-3}$
40 μs - run1	159.2	159.2	39.8	15.8	22	9, 25	$(8.48 \pm 0.94)\times 10^{-3}$
40 μs - run2	159.2	159.2	39.8	15.7	22	9, 25	$(8.58 \pm 0.95)\times 10^{-3}$
40 μs - run3	159.2	159.2	39.8	15.0	22	8, 24	$(10.3 \pm 1.0)\times 10^{-3}$
55 μs - run1	220.4	220.4	55.1	15.9	22	9, 26	$(7.26 \pm 0.74)\times 10^{-3}$
55 μs - run2	220.4	220.4	55.1	16.2	22	9, 26	$(7.57 \pm 0.76)\times 10^{-3}$
55 μs - run3	220.4	220.4	55.1	16.2	22	9, 26	$(7.26 \pm 0.74)\times 10^{-3}$

Data were collected using an RFSoC board equipped with the Quantum Instrumentation Control Kit (QICK) [52]. Detailed setup information, including filtering and amplification stages, are provided in Supplementary Section F. Data corresponding to qubit Q1 were collected both underground at LNGS in 2023 (where the chip was also exposed to radioactive sources) and at FNAL in 2025. At FNAL, we additionally investigated the impact of different sampling periods on the reconstruction of radiation events. To assess the stability of the results over time, we also acquired datasets on different days using identical experimental parameters. A summary of the acquired runs is reported in Table 2.

2.4 Identifying candidate radiation events from qubit measurements

Each experimental run typically lasted several hours, during which hundreds of millions of readouts were recorded. Qubit states were reliably discriminated from the I/Q (in-phase

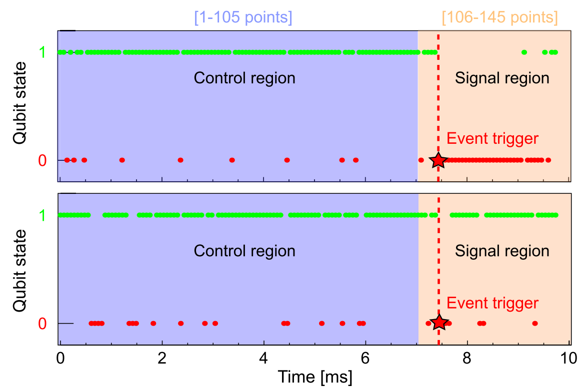

Figure 3 Examples of triggered events. The top panel shows a clear radiation-induced event, identifiable by a significant excess of zeros in the signal region relative to the control region. In contrast, the bottom panel displays a triggered event that was discarded due to the absence of a significant excess of zeros in the signal region. The high level of noise observed in the control region further supports its classification as a noise-induced trigger. These examples illustrate how the combined use of the signal and control regions enables discrimination between genuine radiation-induced events and noise fluctuations

and quadrature-phase) signals, with a typical readout fidelity of 90–95% (see Supplementary Section C for details).

Data were divided into traces of 10^6 measurements (corresponding to approximately one minute of data). Traces exhibiting elevated populations in higher excited states, such as $|f\rangle$ or $|h\rangle$, were excluded from the analysis to ensure robust discrimination between $|g\rangle$ and $|e\rangle$ and maintain data consistency. While transitions involving higher excited states could offer valuable insights for future studies, the current methodology prioritizes a high-purity dataset suitable for quantitative comparison across different runs. This selection reduces the effective live-time of the measurements (Table 2).

For each trace, we obtained a binary sequence of 0s and 1s, corresponding to $|g\rangle$ and $|e\rangle$, respectively. Details of the procedure are provided in Supplementary Section C. To disentangle the 0s originating from radioactivity from those caused by spontaneous qubit decay, we required the detection of at least four consecutive zeros to trigger an event. This criterion reduces false triggers due to spontaneous decay and other noise sources such as electronic noise, vibrations [53, 54] and material relaxation at low temperatures [55, 56]. These effects are particularly relevant at the interface between the holder and the chip [57–59], or in the metallic films [58, 60]. We also repeated the analysis using a trigger threshold of three consecutive zeros and obtained consistent results.

Once an event was triggered, a 145-point window was recorded (see Fig. 3) and divided into two regions:

- **Control region** ($[1, 105]$ points): used to estimate the baseline number of zeros (noise) before the event;
- **Signal region** ($[106, 145]$ points): captured the event, including 5 points before and 35 after the trigger.

The length of the Signal region was chosen through an iterative process. We initially assumed a signal duration of 100 points and performed the analysis described later in the text. Since no events with more than 60 zeros were observed, we reduced the signal window to 60 points. This adjustment preserves the number of zeros generated by radioactivity while reducing the number of zeros from spontaneous qubit decay within the same window. Again, we observed no events with more than 40 zeros in a 60-point window. We therefore further reduced the signal region to 40 points, which was found to be the optimal length to fully capture radiation-induced events while minimizing background noise from spontaneous qubit relaxation. For the device studied here, this corresponds to capturing decay dynamics extending over millisecond timescales. To avoid re-triggering, a dead time of 35 points was applied after each trigger. Figure 3 illustrates two examples of triggered events, one of which was discarded due to not meeting relevant criteria detailed in the next section.

According to the Monte Carlo simulation summarized in Table 1, the event rates due to radioactivity are 0.004 and 0.042 events/sec at LNGS and FNAL, respectively. These values assume that all events interacting with the substrate are successfully detected by the qubit. In practice, however, some detection inefficiency is expected, leading to lower actual rates.

During all Q1 measurements, we observed a ground-state population $P(g)$ ranging from 11.8 to 17.6% (Table 2). A rough estimate suggests that, with this value and a trigger condition requiring four consecutive ground-state measurements, the expected trigger rate due to spontaneous qubit decay is approximately proportional to $P(g)^4/\mathrm{T}_S$ resulting in few events per second (T_S being the sampling period, or the time to complete a cycle). Such a high noise level would completely obscure the 10^{-3} events/sec generated by radioactivity. Therefore, to isolate radiation-induced events after triggering, we apply additional data selection.

Our approach is based on computing the probability of observing more than a certain number of zeros in the signal region. Given a $P(g)$ of about 10%, the most likely values of zeros in a 40-points window would be 3–5 (Binomial distribution). Higher numbers of zeros become less and less probable. Since we expect a rate from radioactivity of few 10^{-3} events/sec, we decided to require the minimum number of zeros in the signal region ($\mathrm{N}_{\mathrm{signal}}^{\mathrm{min}}$) that ensures a noise from qubit decay $<1 \times 10^{-4}$ events/sec, thus an order of magnitude below the searched signal. The precise value of $\mathrm{N}_{\mathrm{signal}}^{\mathrm{min}}$ in the signal region depends on the value of $P(g)$ and the sampling period T_S for that specific run. Since this parameter is rather stable, the values of $\mathrm{N}_{\mathrm{signal}}^{\mathrm{min}}$ to accept an event resulted 21-22 in a 40-points region for most of the Q1 datasets (Table 2).

Similarly, the control region was examined to identify transient noise. Events with an anomalous number of zeros in the control region -indicative of transient noise- were flagged and discarded, as they can lead to false triggers. Specifically, we computed the binomial probability of observing a given number of zeros in the control region and rejected events with a probability lower than 1%. Since both an excess and a deficit of zeros can result in such low probabilities, we selected only events with a number of zeros between $\mathrm{N}_{\mathrm{control}}^{\mathrm{min}}$ and $\mathrm{N}_{\mathrm{control}}^{\mathrm{max}}$ reported in Table 2. The cut was intentionally chosen to be very loose, as its purpose was solely to remove events in which qubit performance deviated significantly from the average. Detailed selection criteria for each dataset are provided in Table 2.

The top panel of Fig. 3 shows a radiation-induced event, where the signal region exhibits a clear excess of zeros compared to the control region. In contrast, the bottom panel displays an event that was subsequently discarded because it does not show a significant excess of zeros in the signal region. These examples highlight the role of the data selection in distinguishing genuine radiation-induced events from noise.

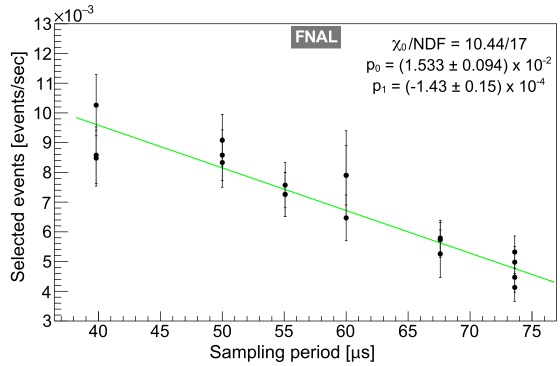

Figure 4 Measured rate of events for FNAL-Q1 as a function of the sampling period. Data were modeled using a first-degree polynomial. The faster the sampling rate, the higher the detection efficiency

2.5 Measured event rates and detection efficiency

The rates of events that passed the data selection procedure (Sect. 2.4), as well as the specific parameters of each run, are listed in Table 2. The runs are reported following the same order in which data were acquired. Each run lasted typically four hours and we often took runs in different days to monitor the stability of the results.

First, we draw the reader's attention to the "FNAL Q1" data, which were acquired using various sampling periods ranging from 40 to 74 µs. We observe that runs with the same sampling period yield consistent results, despite being recorded on different days or with slightly varying qubit lifetimes and hence different values of $P(g)$. Moreover, the data show that shorter sampling periods result in higher measured event rates. Specifically, using a sampling period of 74 µs yields an event rate, averaged over four runs, of $(4.68 \pm 0.26) \times 10^{-3}$ events/sec. When the sampling period is reduced to 40 µs, the event rate, averaged again across the three runs, increases to $(9.08 \pm 0.56) \times 10^{-3}$ events/sec. This trend is also illustrated in Fig. 4, where the event rate is reported as a function of the sampling period.

Such behavior was anticipated. Indeed, for each run, we chose a selection criterion that ensured a qubit decay-induced noise rate below 10^{-4} events/sec, thus keeping the noise rejection efficiency constant. Since the qubit parameters were reasonably reproducible across all measurements, the chosen threshold was more or less the same—typically between 19 and 22 zeros. In contrast, the *signal efficiency* increased with faster sampling periods. For example, if a signal lasts approximately 1.5 milliseconds, a sampling period of 40 µs would produce about 37 zeros, while a 74 µs sampling period would yield only 20. Given that the analysis threshold was set between 19 and 22 zeros (depending on the run), it is likely that events producing only 20 zeros on average have a low signal efficiency. Conversely, events producing 37 zeros would almost always pass the data selection. This effect can be appreciated in Fig. 5, where the two green histograms represent two runs acquired at FNAL with 40 µs and 74 µs sampling period. In the 40 µs run there is a clear excess of events with a large number of 0s. From this study, we conclude that only runs with the same sampling period can be compared.

We now focus on the difference in the event rates measured for Q1 at FNAL and at the underground LNGS laboratory. As previously explained, a meaningful comparison requires the use of the same sampling period. For this reason, we report in Fig. 5 the histograms obtained at both sites utilizing a 74 µs sampling period.

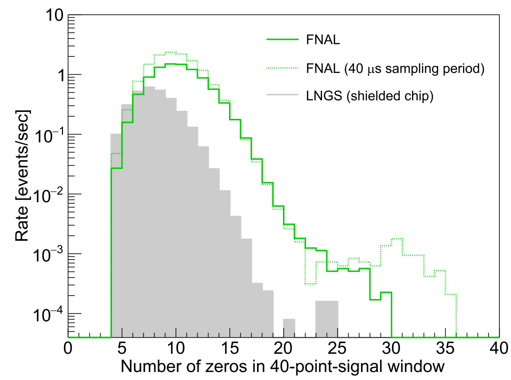

Figure 5 Distribution of zeros in the signal region for runs conducted deep-underground at LNGS (gray, filled histogram) and above-ground FNAL (green lines). At FNAL, the qubits were completely unshielded from cosmic and ambient gamma radiation, resulting in significantly more detected events. The dotted line represents FNAL data acquired with a 40 μs sampling period, while the other FNAL run and the LNGS one were acquired with 74 μs. Runs with different sampling periods are shown to illustrate how this parameter affects detection efficiency; however, only runs with the same sampling period can be directly compared in terms of absolute rates

At LNGS, the "background" run was acquired exclusively with this sampling, yielding a rate of $(0.40 \pm 0.18) \times 10^{-3}$ events/sec. Using the same acquisition parameters at FNAL, we measured an average rate of $(4.68 \pm 0.26) \times 10^{-3}$ events/sec, approximately an order of magnitude higher.

We also note that both the obtained rates are an order of magnitude smaller compared to the prediction of the Monte Carlo simulation (Table 1). This hints that the "detection efficiency" for events produced by ionizing radiation of the protocol developed in this work is around $\sim$10%. The study presented in Fig. 4 indicates that the signal efficiency is limited to approximately 10% primarily due to the sampling period. By repeating the measurement with a shorter sampling period of 40 μs (instead of 74 μs), we nearly doubled the measured signal rate and, consequently, increased the efficiency to 19%. However, we empirically determined that significantly faster sampling rates tend to excite the qubit to its second or third excited states, resulting in non-robust and unreliable measurements.

To further validate these conclusions, we investigated the detection efficiency for events due to ionizing radiation at LNGS by exposing the chip to Thorium radioactive sources with increasing activity levels. For this study, commercially available Thorium rods with known activity were placed between the fridge's outer vacuum chamber and the external Copper shield. Data were analyzed using the same protocol applied to the background runs, and are presented in Fig. 6.

The measured rates indicate that, as expected, exposing the chip to a controlled radioactive source led to an excess of events with a high number of zeros in the signal region compared to the "shielded" configuration. In Fig. 7, the rate of these events is reported as a function of the source's intensity. Since the runs with radioactive sources were performed with a slightly faster sampling period, the rates reported in Table 2 were corrected for this effect (about 10%). We note that directly comparing the background run with the source runs on the same plot is not strictly justified. The presence of the sources could induce unknown effects on the qubit (indeed, the background run is the only one in which we observe such a low $P(g)$), and the energy distribution of the Thorium γ-rays differs from that of the background radiation, as shown in the Supplementary Section B, which

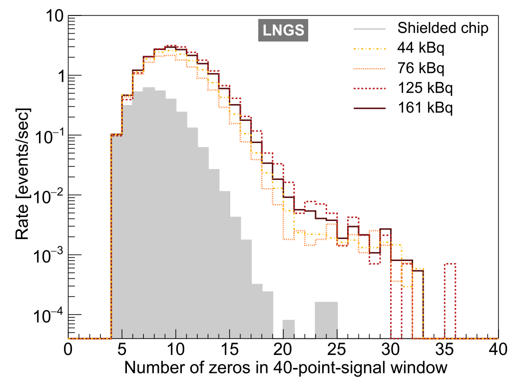

Figure 6 Distribution of zeros in the signal region for runs with controlled radioactive sources at deep-underground LNGS. Data were acquired by exposing the chip to Thorium radioactive sources with increasing activity. For comparison, the distribution for the 'background' run without sources is also shown (light gray)

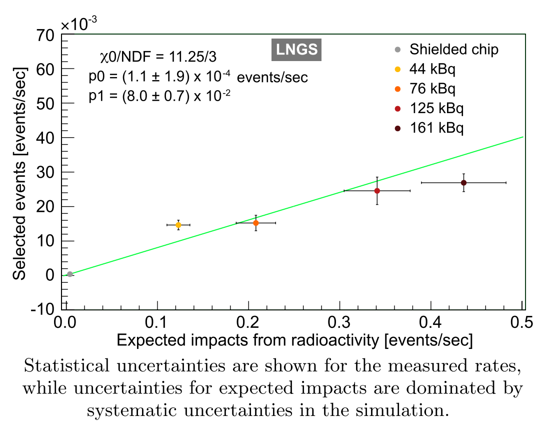

Figure 7 Measured rate of events for LNGS-Q1 as a function of the rate expected from the simulation. The data are modeled using a first-degree polynomial to highlight the dependence of the measured rate on the source activity. The linear coefficient p_1 provides an estimate of the detection efficiency. The figure is intended to illustrate the roughly linear trend rather than a quantitative agreement between measured and simulated rates

may affect the probability for an energy deposition in the substrate to induce a detectable qubit response. Nevertheless, the measured event rates increase roughly linearly with the source activity, demonstrating that the observed excess is induced by ionizing radiation.

Additionally, we compared the triggered and simulated rates for the various Thorium sources. The slope parameter p_1 of the linear fit in Fig. 7 provides an estimate of the detection efficiency of $(8.0 \pm 0.7)\%$ (purely statistical uncertainty), in qualitative agreement with our previous result. While the absolute measured rates are lower than the simulated expectations due to the limited efficiency resulting from the aggressive data selection and the relatively slow sampling period, the monotonic dependence on the source activity remains clearly visible.

3 Discussion

Despite the low detection efficiency, our findings demonstrate that qubits are sensitive to gamma radiation, even though γ-rays deposit less energy compared to cosmic rays [25, 37], providing the first experimental confirmation of the studies conducted in [61]. While the experiments presented in this work show that particle-induced events can be reliably identified, several improvements would be required for superconducting qubits to be effectively used as particle detectors. The detection efficiency achieved in our experiments ($\sim$10%) is far below that of state-of-the-art particle detectors, which typically reach values close to 100% above threshold [62–64]. Nonetheless, the very low energy gap of superconductors makes them inherently sensitive to small energy deposits, with O(meV) sufficient to break Cooper pairs, indicating that higher detection efficiencies are achievable from a theoretical perspective. Significant improvements could be obtained by optimizing both qubit properties and measurement protocol. In particular, a longer and more stable T_1 would reduce $P(g)$, relaxing the analysis threshold and making quasiparticle bursts easier to identify. Increasing the sampling frequency would further enhance sensitivity to fast decay events, as discussed in Sect. 2.5. Taken together, these considerations suggest that superconducting qubits could be exploited as particle detectors with exceptionally low energy thresholds.

Finally, we recall that even triggering on 4 consecutive zeros we obtained a rate of few events/second of single qubit errors, thus orders of magnitude higher compared to the noise induced by radioactivity. This conclusion aligns with recent studies [42], which report that cosmic rays are not the predominant source of the most frequent correlated errors among qubits. The observed radiation-like-induced events could therefore be linked to other mechanisms yet to be fully understood. Investigating these alternative potential sources of correlated errors will be a crucial focus of future studies, aiming to further elucidate the interplay between environmental noise and qubit performance.

In conclusion, we conducted a comparative study to assess the impact of radiation on transmon qubits in two laboratories with very different radiation environments. Standard T_1 measurements on the same qubit revealed no discernible differences in energy relaxation times, which remained consistently around 80 microseconds.

To probe time dynamics at shorter timescales, we developed a fast decay detection protocol with active reset tailored for a single qubit. The same qubit measured with this technique at FNAL (above ground and without Lead and Copper shielding) showed about 10-fold excess rate compared to the maximally shielded qubit at the deep-underground Gran Sasso Laboratory, as predicted by radioactivity studies. However, disentangling such a small excess rate from the single qubit noise required very stringent trigger and analysis thresholds, confirming that radioactivity is not the major source of errors in modern transmon qubits with relaxation times of the order of 0.1 milliseconds.

Experiments with controlled Thorium sources at LNGS demonstrated the potential for detecting γ-ray impacts, opening the possibility of using transmons as particle detectors. However, the observed rates are lower than those predicted by simulations, indicating the need for more refined trigger algorithms and/or analysis strategies. Nevertheless, the approximately linear increase in measured rates with source activity confirms that the detection protocol can reliably identify radiation-induced events, even if absolute rates remain limited by efficiency.

Future work will aim to achieve a deeper understanding of the error sources that currently overshadow radiation-induced effects. This will involve refining fast decay detection and analysis protocols, testing diverse qubit geometries and materials, and conducting simultaneous measurements across both the same and multiple chips. By addressing these challenges, we will move closer to realizing the full potential of transmon qubits in practical quantum technologies.

Supplementary information

Supplementary information accompanies this paper at https://doi.org/10.1140/epjqt/s40507-026-00490-2.

Additional file 1. (PDF 9.1 MB)

Acknowledgements
The authors thank the Director and technical staff of the Laboratori Nazionali del Gran Sasso. We are also grateful to the LNGS Computing and Network Service for computing resources and support on U-LITE cluster at LNGS. We thank S. Nisi for the ICP-MS measurements of the PCB, C. Tomei and G. D'Imperio for the maintenance of the simulation software, G. Catelani for the useful discussion. We are grateful to A. Girardi for the controller of the cryogenic switch, M. Guetti for the help with the whole cryogenic facility (including its continuous upgrades), and M. Iannone for the assembly of the device at LNGS. We are thankful to Theodore C. III and Grzegorz Tatkowski for providing support on experimental preparations and cryogenic operations at FNAL. The work was supported by the U.S. Department of Energy, Office of Science, National Quantum Information Science Research Centers, Superconducting Quantum Materials and Systems (SQMS) Center under the contract No. DE-AC02-07CH11359, by the Italian Ministry of Foreign Affairs and International Cooperation, grant number US23GR09, by the PNRR MUR project CN00000013-ICSC, by the Italian Ministry of Research under the PRIN Contract No. 2020h5l338 ("Thin films and radioactivity mitigation to enhance superconducting quantum processors and low temperature particle detectors") and by the Italian Ministry of Research under the PRIN Contract No. 2022BP4H73 (Chasing Light Dark Matter with Quantum Technologies").

Author contributions
M.B. and F.C. designed and fabricated the transmon devices. S.Z. performed initial characterization of the qubits. A.C. T.R., F.D.D. and D.H. run the experiments. C.B., N.C., F.D.D., F.F., A.M., A.Re., L.C. and M.V. performed the data analysis. D.v.Z. helped in writing acquisition software. A.M. performed GEANT4 simulations. I.C., A.P., L.P., V.P., S.P., A.Ro. and R.P. oversaw the cryostat upgrade for the measurements and the cryogenic operations. T.R., A.M., F.D.D., and L.C. wrote the manuscript with inputs from all the co-authors in interpreting the results. T.R., A.G. and L.C. conceived and supervised the whole project.

Data availability
Data will be made available upon reasonable request.

Declarations

Competing interests
The authors declare no competing interests.

Author details
[1]Gran Sasso Science Institute, L'Aquila I-67100, Italy. [2]Laboratori Nazionali del Gran Sasso, INFN, Assergi, L'Aquila I-67100, Italy. [3]Superconducting Quantum Materials and Systems Center (SQMS), Fermi National Accelerator Laboratory, Batavia, IL 60510, USA. [4]Sezione di Roma, INFN, Rome, I-00185, Italy. [5]Superconducting Quantum Materials and Systems Division, Fermi National Accelerator Laboratory (FNAL), Batavia, IL 60510, USA. [6]Dipartimento di Fisica, Sapienza Università di Roma, Rome, I-00185, Italy. [7]Consiglio Nazionale delle Ricerche, Istituto di Nanotecnologia, Rome, Italy. [8]Illinois Institute of Technology, Chicago, USA.

Received: 15 December 2025 Accepted: 3 March 2026 Published online: 13 March 2026

References

1. Barends R, et al. Superconducting quantum circuits at the surface code threshold for fault tolerance. Nature. 2014;508:500.
2. Arute F, et al. Quantum supremacy using a programmable superconducting processor. Nature. 2019;574:505.
3. Kjaergaard M, Schwartz ME, Braumüller J, Krantz P, Wang JI-J, Gustavsson S, Oliver WD. Superconducting qubits: current state of play. Annu Rev Condens Matter Phys. 2020;11:369.
4. Rigetti aspen-m-2 features. https://www.rigetti.com/what-we-build.
5. Wu Y, et al. Strong quantum computational advantage using a superconducting quantum processor. Phys Rev Lett. 2021;127:180501.
6. Chow J, et al. IBM Quantum breaks the 100-qubit processor barrier. 2021. https://www.ibm.com/quantum/blog/127-qubit-quantum-processor-eagle.
7. Dixit AV, Chakram S, He K, Agrawal A, Naik RK, Schuster DI, Chou A. Searching for dark matter with a superconducting qubit. Phys Rev Lett. 2021;126:141302.

8. Agrawal A, Dixit AV, Roy T, Chakram S, He K, Naik RK, Schuster DI, Chou A. Stimulated emission of signal photons from dark matter waves. Phys Rev Lett. 2024;132:140801.
9. Day PK, LeDuc HG, Mazin BA, Vayonakis A, Zmuidzinas J. A broadband superconducting detector suitable for use in large arrays. Nature. 2003;425:817.
10. Irwin KD. An application of electrothermal feedback for high resolution cryogenic particle detection. Appl Phys Lett. 1995;66:1998.
11. Ullom JN, Bennett DA. Review of superconducting transition-edge sensors for X-ray and gamma-ray spectroscopy. Supercond Sci Technol. 2015;28:084003.
12. Charaev I, et al. Single-photon detection using high-temperature superconductors. Nat Nanotechnol. 2023;18:343.
13. Cardani L, et al. Al/ti/al phonon-mediated kids for uv–vis light detection over large areas. Supercond Sci Technol. 2018;31:075002.
14. Cruciani A, et al. BULLKID: monolithic array of particle absorbers sensed by kinetic inductance detectors. Appl Phys Lett. 2022;121:213504.
15. Mazin BA, Bumble B, Meeker SR, O'Brien K, McHugh S, Langman E. A superconducting focal plane array for ultraviolet, optical, and near-infrared astrophysics. Opt Express. 2012;20:1503.
16. Monfardini A, et al. A dual-band millimeter-wave kinetic inductance camera for the iram 30 m telescope. Astrophys J Suppl Ser. 2011;194:24.
17. Alpert BK, et al. Most stringent bound on electron neutrino mass obtained with a scalable low-temperature microcalorimeter array. Phys Rev Lett. 2025;135:141801.
18. Moretti R, et al. Transmon qubit modeling and characterization for dark matter search. IEEE Trans Quantum Eng. 2026;7:1.
19. Cardani L, et al. Demetra: suppression of the relaxation induced by radioactivity in superconducting qubits. J Low Temp Phys. 2020;199:475.
20. McEwen M, et al. Resisting high-energy impact events through gap engineering in superconducting qubit arrays. Phys Rev Lett. 2024;133:240601.
21. Berritta F, et al. Real-time adaptive tracking of fluctuating relaxation rates in superconducting qubits. 2025. arXiv:2506.09576 [quant-ph].
22. Vepsäläinen AP, et al. Impact of ionizing radiation on superconducting qubit coherence. Nature. 2020;584:551.
23. McEwen M, et al. Resolving catastrophic error bursts from cosmic rays in large arrays of superconducting qubits. Nat Phys. 2021;18:107.
24. Li X, et al. Cosmic-ray-induced correlated errors in superconducting qubit array. Nat Commun. 2025;16:4677.
25. Wilen CD, et al. Correlated charge noise and relaxation errors in superconducting qubits. Nature. 2021;594:369.
26. Thorbeck T, Eddins A, Lauer I, McClure DT, Carroll M. Two-level-system dynamics in a superconducting qubit due to background ionizing radiation. PRX Quantum. 2023;4:020356.
27. Klimov PV, et al. Fluctuations of energy-relaxation times in superconducting qubits. Phys Rev Lett. 2018;121:090502.
28. de Graaf SE, et al. Direct identification of dilute surface spins on $\mathbf{al}_2\mathbf{o}_3$: origin of flux noise in quantum circuits. Phys Rev Lett. 2017;118:057703.
29. Burnett J, et al. Evidence for interacting two-level systems from the 1/f noise of a superconducting resonator. Nat Commun. 2014;5:4119.
30. Bilmes A, et al. Resolving the positions of defects in superconducting quantum bits. Sci Rep. 2020;10:3090.
31. Lisenfeld J, et al. Electric field spectroscopy of material defects in transmon qubits. npj Quantum Inf. 2019;5:105.
32. Martinis JM, et al. Decoherence in Josephson qubits from dielectric loss. Phys Rev Lett. 2005;95:210503.
33. Müller C, et al. Towards understanding two-level-systems in amorphous solids: insights from quantum circuits. Rep Prog Phys. 2019;82:124501.
34. McRae CRH, et al. Materials loss measurements using superconducting microwave resonators. Rev Sci Instrum. 2020;91:091101.
35. Bratrud G, et al. First measurement of correlated charge noise in superconducting qubits at an underground facility. 2024. arXiv:2405.04642.
36. Gusenkova D, et al. Operating in a deep underground facility improves the locking of gradiometric fluxonium qubits at the sweet spots. Appl Phys Lett. 2022;120:054001.
37. Cardani L, et al. Reducing the impact of radioactivity on quantum circuits in a deep-underground facility. Nat Commun. 2021;12. https://doi.org/10.1038/s41467-021-23032-z.
38. Henriques F, et al. Phonon traps reduce the quasiparticle density in superconducting circuits. Appl Phys Lett. 2019;115:212601.
39. Martinis JM. Saving superconducting quantum processors from decay and correlated errors generated by gamma and cosmic rays. npj Quantum Inf. 2021;7:90.
40. Iaia V, et al. Phonon downconversion to suppress correlated errors in superconducting qubits. Nat Commun. 2022;13:6425.
41. Kamenov P, DiNapoli T, Gershenson M, Chakram S. Suppression of quasiparticle poisoning in transmon qubits by gap engineering. 2023. arXiv:2309.02655 [quant-ph].
42. Harrington PM, et al. Synchronous detection of cosmic rays and correlated errors in superconducting qubit arrays. Nat Commun. 2025;16:6428.
43. Cardani L, et al. Disentangling the sources of ionizing radiation in superconducting qubits. Eur Phys J C. 2023;83:94.
44. Orrell JL, Loer B. Sensor-assisted fault mitigation in quantum computation. Phys Rev Appl. 2021;16:024025.
45. Mariani A, et al. Mitigation of cosmic rays-induced errors in superconducting quantum processors. In: IEEEQCE23 proceedings. 2023.
46. Mariani A, et al. A cryogenic muon tagging system based on kinetic inductance detectors for superconducting quantum processors. 2025. arXiv:2512.10679 [quant-ph].
47. Aglietta M, et al (LVD Collaboration). Muon "depth-intensity" relation measured by the lvd underground experiment and cosmic-ray muon spectrum at sea level. Phys Rev D. 1998;58:092005.
48. Yelton E, et al. Modeling phonon-mediated quasiparticle poisoning in superconducting qubit arrays. 2024. arXiv:2402.15471 [quant-ph].

49. Martinez M, Cardani L, Casali N, Cruciani A, Pettinari G, Vignati M. Measurements and simulations of athermal phonon transmission from silicon absorbers to aluminum sensors. Phys Rev Appl. 2019;11:064025.
50. Bal M, et al Systematic improvements in transmon qubit coherence enabled by niobium surface encapsulation. npj Quantum Inf. 2024;10:43.
51. Agostinelli S, et al. GEANT4—a simulation toolkit. Nucl Instrum Methods Phys Res Sect A. 2003;506:250.
52. Stefanazzi L, et al. The qick (quantum instrumentation control kit): readout and control for qubits and detectors. 2022. arXiv:2110.00557 [quant-ph].
53. Kono S, Pan J, Chegnizadeh M, Wang X, Youssefi A, Scigliuzzo M, Kippenberg TJ. Mechanically induced correlated errors on superconducting qubits with relaxation times exceeding 0.4 ms. Nat Commun. 2024;15:3950.
54. Yelton E, Larson CP, Dodge K, Okubo K, Plourde BLT. Correlated quasiparticle poisoning from phonon-only events in superconducting qubits. 2025. arXiv:2503.09554 [quant-ph].
55. Adari P, et al. Excess workshop: descriptions of rising low-energy spectra. 2022. SciPost Phys Proc. https://doi.org/10.21468/scipostphysproc.9.001.
56. Chang CL, et al. Spontaneous generation of athermal phonon bursts within bulk silicon causing excess noise, low energy background events and quasiparticle poisoning in superconducting sensors. 2025. arXiv:2505.16092 [physics.ins-det].
57. Anthony-Petersen R, et al. A stress induced source of phonon bursts and quasiparticle poisoning. 2022. arXiv:2208.02790 [physics.ins-det].
58. Angloher G, et al. Latest observations on the low energy excess in cresst-iii. SciPost Phys Proc. 2023. https://doi.org/10.21468/scipostphysproc.12.013.
59. Armengaud E, et al. Constraints on low-mass wimps from the edelweiss-iii dark matter search. J Cosmol Astropart Phys. 2016;05:019.
60. Romani RK. Aluminium relaxation as the source of excess low energy events in low threshold calorimeters. 2024. arXiv:2406.15425 [physics.ins-det].
61. Fink C, Salemi C, Young B, Schuster D, Kurinsky N. Superconducting quasiparticle-amplifying transmon: a qubit-based sensor for mev-scale phonons and single terahertz photons. Phys Rev Appl. 2024;22:054009.
62. Arnaboldi C, et al. Cuore: a cryogenic underground observatory for rare events. Nucl Instrum Methods Phys Res, Sect A. 2004;518:775–98.
63. Angloher G, et al. Results on light dark matter particles with a low-threshold cresst-ii detector. Eur Phys J C. 2016;76. https://doi.org/10.1140/epjc/s10052-016-3877-3.
64. Pepe C, et al. Detection of low-energy electrons with transition-edge sensors. Phys Rev Appl. 2024;22. https://doi.org/10.1103/physrevapplied.22.l041007.

Publisher's note